ATTITUDE OBSERVABILITY AND OPTIMAL OBSERVATION GEOMETRIES BASED ON SIMULATED LIGHTCURVE OBSERVATIONS FROM AN IDEAL SINGLE FACET TARGET

Zhiying Wang, Anja Schlicht, Manik Reichegger, and Urs Hugentobler

Technische Universität München, 80333 Munich, Germany, Email: {zhiying.wang, anja.schlicht, manik.reichegger, urs.hugentobler}@tum.de

ABSTRACT

Understanding the observability of space debris attitude is crucial for attitude determination with lightcurves. This study examines how observation geometry affects the information content of a single brightness measurement, providing theoretical and intuitive insights into fundamental observability conditions. Assuming an ideal single-facet target, we simulate various spatial configurations to identify optimal observer geometries for both specular and diffuse reflections. The results establish a basis for extending observability analysis to multistatic and time-series scenarios. This work lays the foundation for exploring multiple observation strategies, where integrating data from multiple observers or temporal measurements can further improve attitude determination.

Keywords: lightcurve; attitude obserability; observation geometry.

1. INTRODUCTION

The growing issue of space debris remains a significant concern. Optical telescopes serve as the primary tool for observing space debris, effectively determining orbits but struggling to extract details such as shape, orientation, and reflective properties [1]. Light curves, capturing brightness variations observed by telescopes, offer a cost-effective means to infer these characteristics.

Light Curve Inversion (LCI), extensively developed for asteroids, has been explored for space debris. From 1992 to 2001, Kaasalainen established the standard approach for asteroid LCI [2, 3, 4, 5, 6, 7]. However, space debris differs significantly from asteroids due to its complex reflective properties, necessitating the use of the Bidirectional Reflectance Distribution Function (BRDF) [8, 9, 10, 11]. Additionally, its diverse shapes challenge traditional modeling techniques [12].

To address these complexities, researchers have conducted extensive simulations to understand Resident Space Object (RSO) light curves [13, 14]. Instead of full inversion, partial solutions have been explored, such as Kalman Filtering, Fourier, and Wavelet Transforms for extracting rotational information [15, 16, 17]. More recently, deep learning techniques have been applied to RSO light curve analysis [18, 19, 20, 21].

Beyond these approaches, understanding light curve observability is crucial for extracting meaningful information. Observability quantifies how well light curves reveal parameters such as orientation and reflectance, informing space debris analysis. Hinks formalized the observability of a single brightness measurement, laying the groundwork for further studies [1].

Building on Hinks' framework, this study advances observability analysis by identifying optimal observation geometries. We systematically simulate various single-observation scenarios, providing theoretical and intuitive insights into their impact on observability. This work forms a foundation for extending observability analysis to more complex cases, such as multistatic configurations and time-series measurements.

The remainder of this paper is structured as follows: Section 2 presents the mathematical model for the observability of a single brightness measurement, primarily based on Hinks' work [1]. Section 3 discusses the simulation results under different observational scenarios. Finally, Section 4 summarizes key findings and outlines directions for future research.

2. OBSERVABILITY MODELING

Observability quantifies the sensitivity of the measured brightness to small variations in the object's attitude and surface properties. A rigorous mathematical framework is required to evaluate the observability, as it directly impacts the reliability of shape and attitude reconstruction from optical measurements.

This section establishes the theoretical framework for observability modeling, integrating light propagation and

Proc. 9th European Conference on Space Debris, Bonn, Germany, 1–4 April 2025, published by the ESA Space Debris Office
Editors: S. Lemmens, T. Flohrer & F. Schmitz, (http://conference.sdo.esoc.esa.int, April 2025)

information theory. The BRDF characterizes surface reflection, while the Fisher Information Matrix (FIM) provides a quantitative measure of observability. These formulations assess single-observation observability.

2.1. Light Propagation and BRDF

Table 1. Mathematical symbols used in the formulation.

Symbol	Annotation
$\boldsymbol{e}_{\mathrm{obs}}$	unit vector pointing to reflection direction
$\boldsymbol{e}_{\mathrm{sun}}$	unit vector pointing to incident direction
$\boldsymbol{h}$	half vector, $(\boldsymbol{e}_{\mathbf{sun}} + \boldsymbol{e}_{\mathbf{obs}})/\lVert\boldsymbol{e}_{\mathrm{sun}} + \boldsymbol{e}_{\mathrm{obs}}\rVert$
$\boldsymbol{n}_{(i)}$	normal vector of the i^{th} facet
$c_{on(i)}$	$\boldsymbol{e}_{\mathrm{obs}} \cdot \boldsymbol{n}_{(i)}$
$c_{sn(i)}$	$\boldsymbol{e}_{\mathrm{sun}} \cdot \boldsymbol{n}_{(i)}$
$c_{hn(i)}$	$\boldsymbol{h} \cdot \boldsymbol{n}_{(i)}$
$c_{sh(i)}$	$\boldsymbol{e}_{\mathrm{sun}} \cdot \boldsymbol{h}$
r	surface roughness, higher means smoother
R_s	specular reflectance at normal incidence
R_d	diffuse reflectance

Observability modeling relies on representing observations of non-luminous objects like space debris, where measurements correspond to sunlight reflected from their surfaces. This process consists of two key components: light propagation from the Sun to the telescope and the target's surface reflection characteristics.

Consider a space debris target with k facets, where the i^{th} facet has an area $\mathcal{A}(i)$. The light propagation path, or observation geometry, of this facet is illustrated in Fig. 1, with vector definitions provided in Tab. 1.

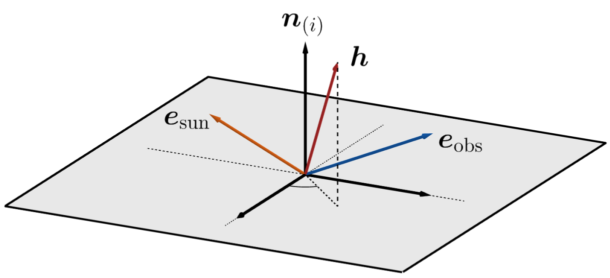

Figure 1. Observation geometry on the i^{th} facet

By applying approximations, light propagation modeling is simplified. Since orbital elevation variations are negligible relative to the Earth-Sun distance, the solar radiation received by space debris is assumed uniform, approximated by the solar constant C_{sun}. Accounting for atmospheric effects, the energy density at the telescope, isolating reflection and distance factors, is given by $C_{\mathrm{sun,vis}}$.

Thus the irradiance received by the observer is given as Eq. (1):

$$E_{\mathrm{obs}(i)} = C_{\mathrm{sun,vis}} \cdot \rho_{(i)} \cdot \mathcal{A}_{(i)} \frac{c_{sn(i)} \cdot c_{on(i)}}{d^2} \tag{1}$$

where d is the distance between the target and the observer, and $\rho_{(i)}$ is the BRDF of the i^{th} facet. The BRDF models surface reflection by relating reflected radiance to incident irradiance based on illumination and viewing geometry. It is a fundamental tool for characterizing reflection properties in light propagation.

Following Hinks [1], we adopt the Ashikhmin-Shirley BRDF model [11, 10, 9], which captures both specular and diffuse reflections. The surface parameters used in this model are listed in Tab. 1. The BRDF of the i^{th} facet is given by Eq. (2):

$$\rho_{(i)} = \rho_{s(i)} + \rho_{d(i)} \tag{2}$$

The first part $\rho_{s(i)}$ is for specular component:

$$\begin{aligned}\rho_{s(i)} = \frac{r+1}{8\pi} \cdot & \frac{c_{hn(i)}^{z_{(i)}}}{c_{sn(i)} + c_{on(i)} - c_{sn(i)} \cdot c_{on(i)}} \\ & \cdot \left[R_s + (1-R_s)\left(1 - c_{sh(i)}\right)^5\right]\end{aligned} \tag{3}$$

where the exponent z can be written as:

$$z_{(i)} = \frac{r_{(i)}}{1 - c_{hn(i)}^2} \tag{4}$$

The second part $\rho_{d(i)}$ is for diffuse component:

$$\begin{aligned}\rho_{d(i)} = k_{(i)} & \left[1 - \left(1 - \frac{c_{sn(i)}}{2}\right)^5\right] \\ & \cdot \left[1 - \left(1 - \frac{c_{on(i)}}{2}\right)^5\right]\end{aligned} \tag{5}$$

where the scale factor $k_{(i)}$ can be written as:

$$k_{(i)} = \frac{28 R_{d(i)}}{23\pi}\left(1 - R_{s(i)}\right) \tag{6}$$

In summary, by integrating the light propagation model in Eq. (1) with the BRDF model formulated in Eqs. (2) to (6), we complete the modeling of the light curve observations.

2.2. Fisher Information Matrix and Observability

The Fisher Information Matrix (FIM) quantifies how observations $\boldsymbol{x}$ constrain unknown parameters $\boldsymbol{\mu}$, establishing a theoretical bound on estimation precision. Given a functional relationship h, the observation model is:

$$\boldsymbol{x} = h(\boldsymbol{\mu}) + \boldsymbol{\varepsilon} \tag{7}$$

where ε represents observation noise with a covariance matrix $\mathcal{R} = \varepsilon\varepsilon^T$.

Following Hinks [1], the FIM of $\boldsymbol{\mu}$ given observations $\boldsymbol{x}$ is formulated as:

$$\boldsymbol{F}(\boldsymbol{\mu}) = \left(\frac{\partial h}{\partial \boldsymbol{\mu}}\right)^T \mathcal{R}^{-1} \left(\frac{\partial h}{\partial \boldsymbol{\mu}}\right) \tag{8}$$

which quantifies how observation sensitivity and noise determine the best achievable estimation precision, commonly referred to as observability.

From Eq. (8), attitude observability from light curves requires computing the gradient of observed irradiance with respect to attitude parameters, given by [1]:

$$\begin{aligned}\frac{\partial E_{\text{obs}}}{\partial \boldsymbol{\delta\alpha}} = \sum_{i=1}^{N} E_{\text{obs}(i)} \Big[& C_{n1(i)} \left(\boldsymbol{e}_{\text{obs}} \times \boldsymbol{n}_{(i)}\right)^T \\ & + C_{n2(i)} \left(\boldsymbol{e}_{\text{sun}} \times \boldsymbol{n}_{(i)}\right)^T \Big]\end{aligned} \tag{9}$$

where the scale factors $C_{n1(i)}$ and $C_{n2(i)}$ can be written as:

$$\begin{aligned} C_{n1(i)} = & \frac{\rho_{s(i)}}{\rho_{(i)}} \left[\frac{z_{(i)}}{c_{sum(i)}} - \frac{1 - c_{sn(i)}}{c_{sum(i)} - c_{prod(i)}} \right] \\ & + \frac{5k_{(i)}}{2\rho_{(i)}} \left[1 - \left(1 - \frac{c_{sn(i)}}{2}\right)^5 \right] \left[1 - \frac{c_{on(i)}}{2} \right]^4 \\ & + \frac{1}{c_{on(i)}} \\ C_{n2(i)} = & \frac{\rho_{s(i)}}{\rho_{(i)}} \left[\frac{z_{(i)}}{c_{sum(i)}} - \frac{1 - c_{on(i)}}{c_{sum(i)} - c_{prod(i)}} \right] \\ & + \frac{5k_{(i)}}{2\rho_{(i)}} \left[1 - \left(1 - \frac{c_{on(i)}}{2}\right)^5 \right] \left[1 - \frac{c_{sn(i)}}{2} \right]^4 \\ & + \frac{1}{c_{sn(i)}} \end{aligned} \tag{10}$$

The notation used to simplify expressions in Eq. (10) is given by Eq. (11):

$$\begin{aligned} c_{sum(i)} &= c_{on(i)} + c_{sn(i)} \\ c_{prod(i)} &= c_{on(i)} c_{sn(i)} \end{aligned} \tag{11}$$

Thus, by substituting Eq. (9) into Eq. (8), the FIM for the attitude parameters can be formulated as:

$$\boldsymbol{F}(\boldsymbol{\delta\alpha}) = \left(\frac{\partial E_{\text{obs}}}{\partial \boldsymbol{\delta\alpha}}\right)^T \mathcal{R}^{-1} \left(\frac{\partial E_{\text{obs}}}{\partial \boldsymbol{\delta\alpha}}\right) \tag{12}$$

3. OBSERVABILITY OF SIMULATED DATA

Our objective is to investigate how observation geometry influences attitude observability, providing a deeper understanding of the relationship between observation geometry and the information content of light curve measurements.

To achieve this, we simulate various observation geometries for a single observation scenario, modeling the target as an ideal single-facet object. These simulations offer both theoretical and intuitive insights into how different spatial arrangements affect observability, laying the foundation for further discussions on optimizing observation strategies.

3.1. Simulation Configurations

The simulations are configured with defined coordinate systems, BRDF parameters, rotation settings for time-series analysis, and necessary simplifications to reflect practical observation conditions.

It is essential to highlight that, to simplify the analysis and provide a clearer understanding of the physical implications of observability, all simulations are conducted based on an idealized single reflective facet target, with area of 1 square meter.

3.1.1. Coordinate System

To ensure consistency in observation modeling, we define a unified coordinate system framework. The inertial coordinate system serves as the global reference frame, describing the space debris target's orientation, while the body-fixed coordinate system, aligned with its surface normal vectors, is used to describe the observation geometry.

Since only a single observation is considered, absolute positions of the target, observers, and the Sun are irrelevant. Instead, their relative directions are adjusted to simulate different observation geometries. A polar coordinate system centered on the target's body frame is used for this purpose, facilitating the computation of incidence and reflection angles.

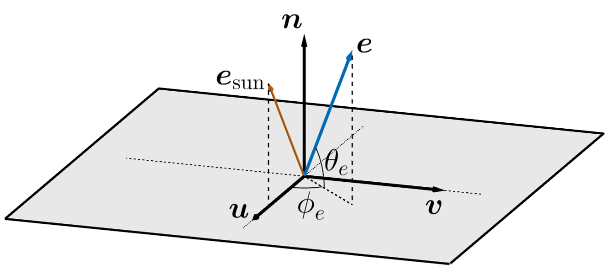

Figure 2. Polar coordinate system for simulations.

As shown in Fig. 2, an arbitrary direction vector in the body frame $\boldsymbol{e}$ is expressed using its azimuth $\phi_{\boldsymbol{e}}$ and elevation $\theta_{\boldsymbol{e}}$. As the ideal single-facet target is assumed to have isotropic surface properties, there is no inherent reference for the azimuth. Thus, we define $\phi = 0$ as the azimuth of the Sun. These angle notations are retained for subsequent discussions.

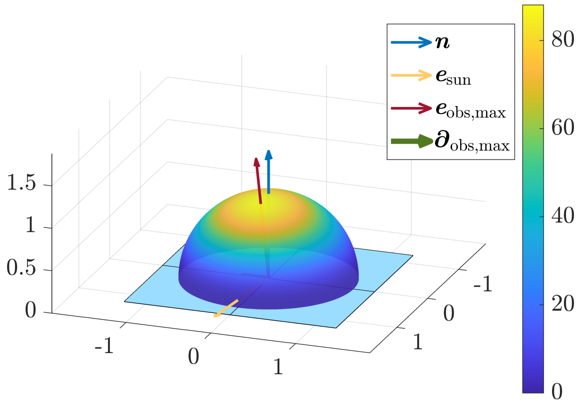

(a) Observability distribution

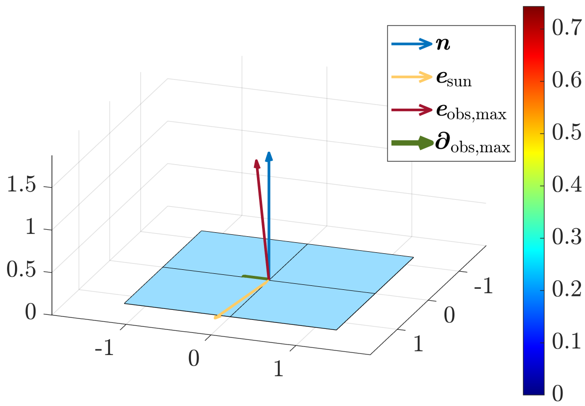

(b) BRDF lobe

Figure 3. Diffuse component of a single epoch monostatic observation, $\theta_{\text{sun}} = 5°$.

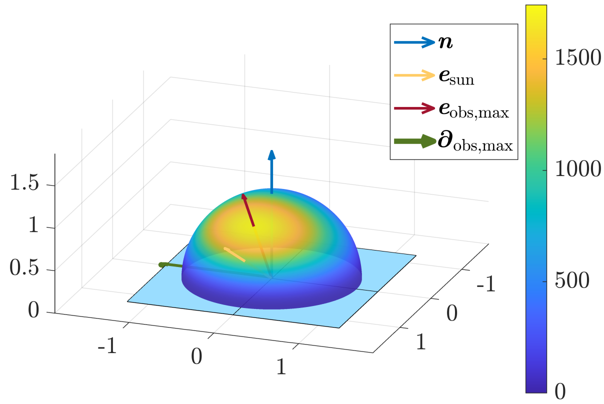

(a) Observability distribution

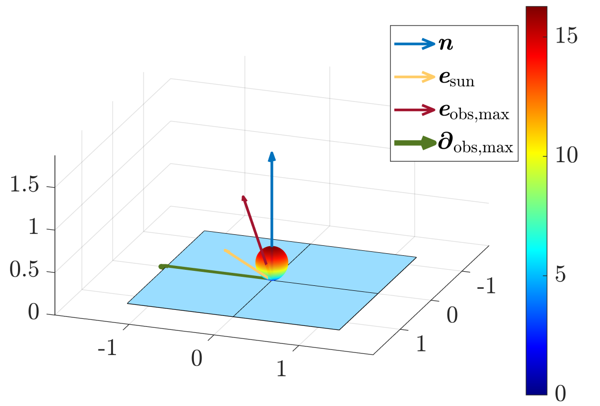

(b) BRDF lobe

Figure 4. Diffuse component of a single epoch monostatic observation, $\theta_{\text{sun}} = 30°$.

3.1.2. BRDF Parameters

In our simulation, the target's surface properties are defined by BRDF parameters, including r for surface roughness, R_s for specular reflectance, and R_d for diffuse reflectance, as listed in Tab. 1.

Space debris, often originating from fragmented spacecraft, is typically covered with highly reflective multi-layer insulation, resulting in smooth optical characteristics. To approximate this, we set $r = 1000$, effectively modeling a smooth surface. Due to the lack of publicly available reflectance data for spacecraft materials, we assume an equal distribution between specular and diffuse reflection, assigning $R_s = R_d = 0.5$ as a reasonable approximation.

3.2. Simulation Results

Initially we simulated just one measurement of a single epoch, for a monostatic telescope it means we only have one brightness measurement.

Given the assumption of a smooth target surface, the specular component of the BRDF is confined to a small region. When the observer's direction falls far from this region, diffuse reflection dominates. Due to the large magnitude difference between specular and diffuse components, the latter becomes indistinguishable when both are considered together. Thus, we analyze the diffuse and the specular components separately. This applies to all subsequent scenarios.

3.2.1. Diffuse Reflection Component

Figs. 3 to 6 illustrate the observability from the diffuse components of single-epoch observations in a monostatic system, where the solar elevation angle varies from 5° to 90°. The light blue plane represents the ideal single-facet reflective target, with the dark blue vector $\boldsymbol{n}$ indicating its surface normal. The yellow vector $\boldsymbol{e}_{\text{sun}}$ denotes the Sun's direction, while the dark red vector $\boldsymbol{e}_{\text{obs,max}}$ represents the observer direction that maximizes observability under the given conditions. The dark green vector $\boldsymbol{\partial}_{\text{obs,max}}$ corresponds to the optimal gradient of the observed value with respect to attitude. A simplified notation is used here for gradients and will be maintained. The hemispheres or lobes visualize the distribution of observability or BRDF relative to the observer's direction.

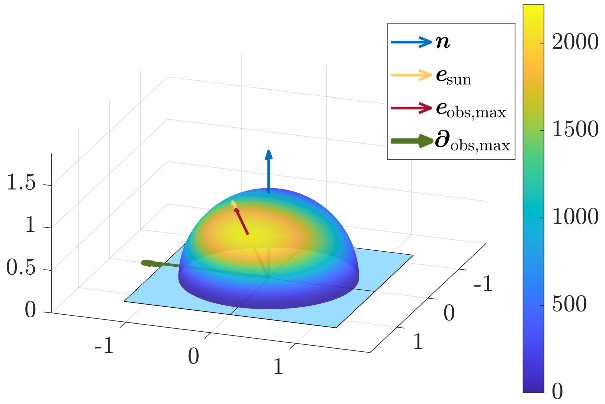

(a) Observability distribution

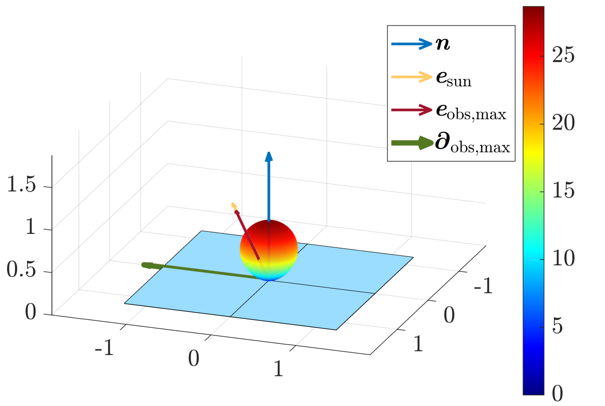

(b) BRDF lobe

Figure 5. Diffuse component of a single epoch monostatic observation, $\theta_{\text{sun}} = 48°$.

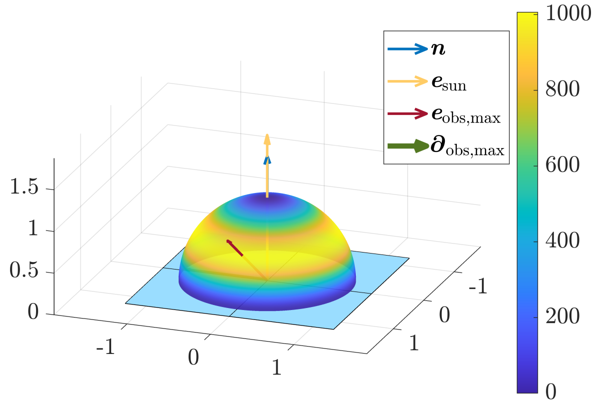

(a) Observability distribution

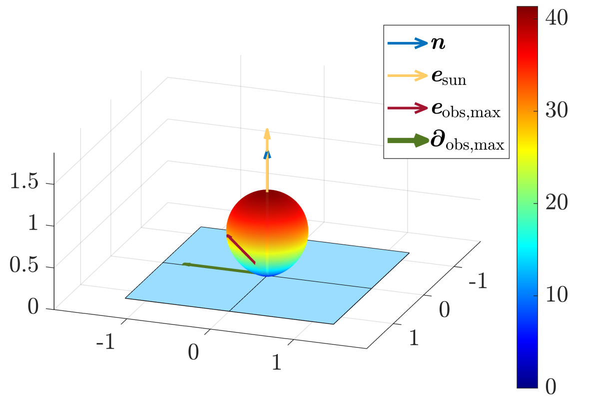

(b) BRDF lobe

Figure 6. Diffuse component of a single epoch monostatic observation, $\theta_{\text{sun}} = 90°$.

Notably, due to the large variations in observability and BRDF values across different observation geometries, a dynamic numerical range is applied to ensure clarity in their distributions, as indicated by the color scale on the right side of each figure. Additionally, since a polar coordinate system is used, the scale values on the XYZ axes have no actual significance and serve only to indicate axis orientation.

The first notable phenomenon is that the maximum observability consistently occurs at the observer azimuth of 0°. This is because when the Sun and the observer are aligned with the target, the projected area in light propagation experiences minimal surface area loss.

However, this trend differs for the observer's elevation. Regarding the observer's elevation, as θ_{sun} increases, the observer direction yielding the highest observability shifts lower. Explaining this requires examining the observation expression in Eq. (1) with the diffuse BRDF component in Eq. (5). Neglecting the specular component and constant coefficients, we obtain:

$$
\begin{aligned}
E_{\text{obs,diff}} = &\left[1 - \left(1 - \frac{\boldsymbol{e}_{\text{sun}} \cdot \boldsymbol{n}}{2}\right)^5\right] (\boldsymbol{e}_{\text{sun}} \cdot \boldsymbol{n}) \\
&\cdot \left[1 - \left(1 - \frac{\boldsymbol{e}_{\text{obs}} \cdot \boldsymbol{n}}{2}\right)^5\right] (\boldsymbol{e}_{\text{obs}} \cdot \boldsymbol{n})
\end{aligned}
\tag{13}
$$

This equation shows that the diffuse component is primarily governed by the cosine of the zenith angles of the Sun and the observer. Expressing these angles as functions of $\boldsymbol{\delta\alpha}$, we define:

$$
\begin{aligned}
\mathcal{S}(\boldsymbol{\delta\alpha}) &= \left[1 - \left(1 - \frac{\boldsymbol{e}_{\text{sun}} \cdot \boldsymbol{n}}{2}\right)^5\right] (\boldsymbol{e}_{\text{sun}} \cdot \boldsymbol{n}) \\
\mathcal{O}(\boldsymbol{\delta\alpha}) &= \left[1 - \left(1 - \frac{\boldsymbol{e}_{\text{obs}} \cdot \boldsymbol{n}}{2}\right)^5\right] (\boldsymbol{e}_{\text{obs}} \cdot \boldsymbol{n})
\end{aligned}
\tag{14}
$$

Thus, E_{obs} can be rewritten as:

$$
E_{\text{obs,diff}} = \mathcal{S}(\boldsymbol{\delta\alpha}) \cdot \mathcal{O}(\boldsymbol{\delta\alpha}) \tag{15}
$$

Taking the derivative, we obtain:

$$
\frac{\partial E_{\text{obs,diff}}}{\partial \boldsymbol{\delta\alpha}} = \mathcal{S}(\boldsymbol{\delta\alpha})\, \mathcal{O}'(\boldsymbol{\delta\alpha}) + \mathcal{S}'(\boldsymbol{\delta\alpha})\, \mathcal{O}(\boldsymbol{\delta\alpha}) \tag{16}
$$

Using Eq. (16), we can interpret the variations in observability with respect to the Sun's and observer's elevations. When $\theta_{\text{sun}} = 90°$, $\mathcal{S}(\boldsymbol{\delta\alpha})$ reaches its maximum, corresponding to the largest projected area and the broadest BRDF lobe, while $\mathcal{S}'(\boldsymbol{\delta\alpha}) = 0$, as shown in Fig. 6. A similar behavior applies to $\mathcal{O}(\boldsymbol{\delta\alpha})$ concerning the observer's elevation. When $\theta_{\text{obs}} = 90°$, $\mathcal{O}(\boldsymbol{\delta\alpha})$ attains its peak value with the largest projected area and highest BRDF contribution, while $\mathcal{O}'(\boldsymbol{\delta\alpha}) = 0$, as seen in Fig. 3.

As θ_{sun} increases from 0° to 90°, $\mathcal{S}(\boldsymbol{\delta\alpha})$ grows, while $\mathcal{S}'(\boldsymbol{\delta\alpha})$ diminishes. At the same time, $\mathcal{O}'(\boldsymbol{\delta\alpha})$ becomes increasingly dominant, while $\mathcal{O}(\boldsymbol{\delta\alpha})$ plays a lesser role, as illustrated in Figs. 4 and 5.

This explains why the observer elevation corresponding to maximum observability decreases as the Sun's elevation rises. Additionally, it clarifies why the maximum observability first increases and then decreases with increasing solar elevation. When the magnitudes and gradients of $\mathcal{S}(\boldsymbol{\delta\alpha})$ and $\mathcal{O}(\boldsymbol{\delta\alpha})$ reach a balanced trade-off, the overall gradient—and thus the observability—achieves its peak, as demonstrated in Fig. 5.

3.2.2. Specular Reflection Component

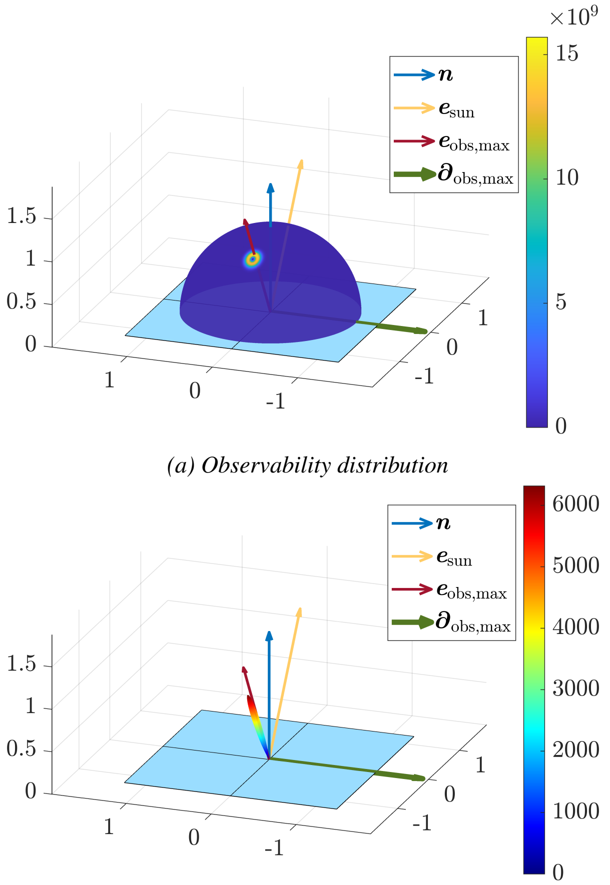

(a) Observability distribution

(b) BRDF lobe

Figure 7. Specular component of time-series monostatic observations, $\theta_{\text{sun}} = 55°$.

Fig. 7 illustrates the observability from the specular component of a single-epoch observation in a monostatic system. It need to be noted that due to the significant numerical disparity between the specular and diffuse components of the BRDF, Fig. 7 applies a different normalization factor for the BRDF lobe visualization and gradient vector lengths compared to Figs. 3 to 6. Consequently, their sizes or lengths depicted in the figures are not directly comparable.

Since specular reflection is concentrated within a small region, as seen in Fig. 7b, the optimal observer direction becomes more distinct and easier to interpret. This results in a distinct ring-like region around the specular lobe, as shown in Fig. 7a, where brightness variations are most significant.

When the observer is positioned within this ring, even minor attitude variations of the target lead to significant changes in the observed light curve, making this region the most informative. Compared to Fig. 5, where diffuse reflection is the primary contributor, Fig. 7 shows that the maximum observability in the specular component is exponentially higher.

Moreover, the observer direction with maximum observability does not only lie along this ring but also consistently aligns with the midpoint of its upper half, corresponding to the highest elevation. To explain this, we can reconsider Eq. (1) from another perspective. By isolating the area projection coefficients from the BRDF, while neglecting constant terms, we define:

$$E_{\text{obs,spec}} = \rho_s \cdot (c_{sn} \cdot c_{on}) = \rho_s(\boldsymbol{\delta\alpha}) \cdot \mathcal{C}_{proj}(\boldsymbol{\delta\alpha}) \quad (17)$$

where $\mathcal{C}_{proj}$ represents the area projection coefficients.

Following a similar approach to Eq. (16), we compute the gradient:

$$\frac{\partial E_{\text{obs,spec}}}{\partial \boldsymbol{\delta\alpha}} = \rho_s(\boldsymbol{\delta\alpha}) \cdot \mathcal{C}'_{proj}(\boldsymbol{\delta\alpha}) + \rho'_s(\boldsymbol{\delta\alpha}) \cdot \mathcal{C}_{proj}(\boldsymbol{\delta\alpha}) \quad (18)$$

This formulation clarifies why the highest elevation point along the specular ring exhibits the greatest observability. Within this region, $\rho'_s(\boldsymbol{\delta\alpha})$ dominates the gradient magnitude, with $\mathcal{C}_{proj}(\boldsymbol{\delta\alpha})$ acting as a scaling factor. Higher elevation angles result in larger area projection coefficients, amplifying $\rho'_s(\boldsymbol{\delta\alpha})$ and ultimately leading to a greater overall gradient and enhanced observability.

4. CONCLUSION

This study explored the observability of space debris attitude through simulated light curve observations, emphasizing the impact of observation geometry on the information content of measurements. By extending previous works on attitude observability, we systematically analyzed the optimal observation conditions to enhance the possibility of attitude determination of space debris. Our findings indicate that the observer's relative direction with respect to the Sun and target significantly influences the observability of attitude. Specifically, we demonstrated the optimal observer geometries for both specular and diffuse reflection components.

These results lay a solid foundation for further investigations into more complex observational configurations, such as multistatic setups and time-series analysis, where multiple observers or temporal measurements contribute to attitude determination. By characterizing the fundamental observability conditions, this study provides a basis for extending attitude obserability frameworks to incorporate diverse observation strategies, ultimately improving our understanding of space debris dynamics in more generalized scenarios.

ACKNOWLEDGMENTS

The authors would like to express their sincere gratitude to the Bundesministerium für Wirtschaft und Klimaschutz (BMWK) for funding this research under Grant No. 50LZ2204 for the project "Multistatische Lichtkurven: Analyse der Komplementarität der Messinformation."

Gefördert durch:

Bundesministerium
für Wirtschaft
und Klimaschutz

aufgrund eines Beschlusses
des Deutschen Bundestages

We also acknowledge Technische Universität München – Forschungseinrichtung Satellitengeodäsie for their support and access to essential resources. Special thanks go to our colleagues and collaborators for their valuable discussions and contributions to the analysis.

REFERENCES

1. Joanna Hinks, Richard Linares, and John Crassidis, 2013, *Attitude Observability from Light Curve Measurements*. In: *AIAA Guidance, Navigation, and Control (GNC) Conference*. Aug. 2013. ISBN: 978-1-62410-224-0.
2. H. N. Russell, 1906, *On the light variations of asteroids and satellites*. In: *Astrophys. J.* **24** (July 1906), pp. 1–18. ISSN: 0004-637X.
3. Steven J. Ostro and Robert Connelly, 1984, *Convex profiles from asteroid lightcurves*. In: *Icarus* **57**.3 (1984), pp. 443–463. ISSN: 0019-1035.
4. M. Kaasalainen et al., 1992, *Interpretation of lightcurves of atmosphereless bodies. I - General theory and new inversion schemes*. In: *Astron. Astrophys.* **259**.1 (June 1992), pp. 318–332. ISSN: 0004-6361.
5. M. Kaasalainen, L. Lamberg, and K. Lumme, 1992, *Interpretation of lightcurves of atmosphereless bodies. II - Practical aspects of inversion*. In: *Astron. Astrophys.* **259**.1 (June 1992), pp. 333–340. ISSN: 0004-6361.
6. M. Kaasalainen and J. Torppa, 2001, *Optimization Methods for Asteroid Lightcurve Inversion: I. Shape Determination*. In: *Icarus* **153**.1 (2001), pp. 24–36. ISSN: 0019-1035.
7. M. Kaasalainen, J. Torppa, and K. Muinonen, 2001, *Optimization Methods for Asteroid Lightcurve Inversion: II. The Complete Inverse Problem*. In: *Icarus* **153**.1 (2001), pp. 37–51. ISSN: 0019-1035.
8. Doyle Hall et al., 2007, *Separating attitude and shape effects for non-resolved objects*. In: *The 2007 AMOS Technical Conference Proceedings*. Maui Economic Development Board, Inc. Kihei, Maui, HI. 2007, pp. 464–475.
9. Michael Ashikmin, Simon Premože, and Peter Shirley, 2000, *A Microfacet-Based BRDF Generator*. In: *Proceedings of the 27th Annual Conference on Computer Graphics and Interactive Techniques*. SIGGRAPH '00. USA: ACM Press/Addison-Wesley Publishing Co., 2000, pp. 65–74. ISBN: 1581132085.
10. Michael Ashikhmin and Peter Shirley, 2001, *An anisotropic phong BRDF model*. In: *Journal of Graphics Tools* **5** (Jan. 2001).
11. Michael Ashikhmin and Simon Premoze, 2007, *Distribution-based brdfs*. In: *Unpublished Technical Report, University of Utah* **2** (2007), p. 6.
12. Ben K Bradley and Penina Axelrad, 2014, *Lightcurve inversion for shape estimation of geo objects from space-based sensors*. In: *Univ. of Colorado. International Space Symposium for Flight Dynamics*. 2014.
13. H. Cowardin et al., 2009, *An Assessment of GEO Orbital Debris Photometric Properties Derived from Laboratory-Based Measurements*. In: *Advanced Maui Optical and Space Surveillance Technologies Conference* (2009), E25.
14. Daniel Burandt et al., 2017, *Interpretation of light curves based on simulation software*. In: *Proceedings of the 68th International Astronautical Congress (IAC), Adelaide, Australia*. 2017, pp. 25–29.
15. Charles J. Wetterer and Moriba Jah, 2009, *Attitude Determination from Light Curves*. In: *Journal of Guidance, Control, and Dynamics* **32**.5 (2009), pp. 1648–1651.

16. Doyle Hall and Paul Kervin, 2014, *Optical characterization of deep-space object rotation states*. In: *2014 AMOS Conference, Maui, HI*. 2014, pp. 9–12.

17. Andrew Dianetti and John Crassidis, 2018, *Light Curve Analysis Using Wavelets*. In: Jan. 2018.

18. Roberto Furfaro, Richard Linares, and Vishnu Reddy, 2019, *Shape identification of space objects via light curve inversion using deep learning models*. In: *AMOS Technologies Conference, Maui Economic Development Board, Kihei, Maui, HI*. 2019.

19. Gregory Badura et al., 2021, *Multi-Scale Convolutional Neural Networks for Inference of Space Object Attitude Status from Detrended Geostationary Light Curves*. In: Feb. 2021.

20. Walter D. Bennette, Kayla Zeliff, and Joseph Raquepas, 2017, *Classification of objects in geosynchronous earth orbit via light curve analysis*. In: *2017 IEEE Symposium Series on Computational Intelligence (SSCI)*. 2017, pp. 1–6.

21. Gregory P. Badura, Christopher R. Valenta, and Brian Gunter, 2022, *Convolutional Neural Networks for Inference of Space Object Attitude Status*. In: *J. Astronaut. Sci.* **69**.2 (Apr. 2022), pp. 593–626. ISSN: 2195-0571.